Simulation of materials-processing plasmas

By Edward P. Hammond, Krishnan Mahesh AND Parviz Moin

1. Motivation and objectives

Plasmas exhibit a rich variety of complex, non-linear behavior and are heavily used in industry. Applications of plasma processing are quite broad; the ability of a chemically active plasma to change the surface properties of materials plays a key role in such industries as aerospace, automotive, steel, biomedical, and toxic waste management (see Lieberman & Lichtenberg 1994 and Grill 1994 for examples).

The semiconductor manufacturing industry uses processing plasmas extensively. Plasmas are used to etch extremely fine features in silicon wafers; feature sizes are currently on the order of 0.18 μm and are anticipated to decrease to 0.05 μm by 2012, according to the semiconductor industry's "National Technology Roadmap" (Hershkowitz 1998). Plasmas are also used in integrated circuit fabrication to deposit thin films and clean residual material from the circuits ("ashing").

The design of plasma reactors includes, but is not limited to, the plasma generation mechanism (the coupling of the electrical power to the plasma), the plasma chemistry (the composition of the feedstock gases), and the operating conditions (pressure and flowrate of the feed gases). The various types of commercial reactors are discussed by Lieberman & Lichtenberg (1994) and Hershkowitz (1998). Semiconductor manufacturing technology is constantly evolving, and designers have to deal with fundamental problems such as plasma uniformity and contamination of the plasma by dust (Hershkowitz 1998).

The development of numerical models to simulate processing plasmas has been ongoing for over two decades, with the most rapid growth occurring during the past decade. Prior to 1990, simulations were typically one-dimensional, either with a fluid model or a particle model of the plasma; since then, two- and three-dimensional models with detailed chemistry have been developed (Kushner 1996). These tools, most of which were developed in academia or the national laboratories, are actually being used by industry as part of the design process (Kushner 1996).

The objective of this work is to develop a conservative numerical algorithm that provides a robust, rapid, and accurate solution to the plasma fluid equations. This report examines a low-pressure, low-temperature, glow discharge He plasma with a very small ionization fraction ($\approx 10^{-8}$). The plasma is maintained in a capacitively-coupled reactor; this type of reactor is frequently used for materials processing purposes.

2. Accomplishments

A conservative, time-accurate algorithm that provides rapid solutions to the plasma fluid equations was developed. Care was taken to ensure that the algorithm is not numerically dissipative. A one-dimensional radio-frequency, capacitive

FIGURE 1. A schematic of a one-dimensional, capacitively-coupled plasma reactor. The plasma bulk is the light gray region, and the dark gray regions represent the plasma sheaths. The reactor is driven by the radio-frequency voltage applied to the left-hand electrode. The sheaths form and collapse throughout the radio-frequency period.

He discharge was used for validation purposes. As will be seen, even this one-dimensional problem poses significant challenges: it has a wide range of time-scales, steep unsteady gradients in charged particle densities, and near-zero electron densities in the sheaths. Upwind biasing the spatial discretization is commonly used to circumvent the problems posed by steep gradients at the sheath edges and very low electron densities (see, for example, Sommerer & Kushner 1992; Gogolides *et al.* 1992, and Kushner *et al.* 1996). However, it will be seen (section 2.3) that upwinded solutions on coarse grids can be quite inaccurate. A non-dissipative discretization based on a rearranged form of the electron flux term was derived. Coarse-grid solutions are seen to be noticeably more accurate than an upwinded scheme with the same computational stencil. The implicit temporal discretization was evaluated for both cost and accuracy. Unsteady solutions to the one-dimensional problem are currently obtained in about 10 minutes on a SGI Iris Indigo 2 workstation. This makes three-dimensional calculations feasible. The algorithm is currently being implemented in a three-dimensional solver with more detailed physics.

2.1 Plasma model

Generally speaking, processing plasmas are sustained by the highly energetic electrons which collide with the background gas to generate ions and more electrons. Power is input to the electrons in a capacitive discharge via the applied radio frequency voltage. A sketch of a one-dimensional capacitive discharge is shown in Fig. 1. Since the characteristic frequency of the ions ($\frac{1}{2\pi}\omega_i = \frac{1}{2\pi}\sqrt{e^2 n_i/\epsilon_0 m_i} \approx$ 3 MHz) is lower than the radio frequency (12 MHz in this report), the ion variables change little during a period. In contrast, the characteristic frequency of the electrons ($\frac{1}{2\pi}\omega_e = \frac{1}{2\pi}\sqrt{e^2 n_e/\epsilon_0 m_e} \approx 300$ MHz) is much higher than the radio frequency. As a result, the electrons are subject to significant changes during a period. On the whole, the plasma is electrically neutral with thin sheaths forming near the boundaries. These sheaths form because the lighter electrons quickly diffuse away, which creates a net positive charge and an electric field that acts to prevent further electrons from escaping. Sheaths in a capacitive radio-frequency discharge are extremely unsteady. A more complete description of the physics of a processing plasma may be found in Lieberman & Lichtenberg (1994).

The fluid equations for a plasma are derived from the Boltzmann equation for each species by specifying the velocity distribution function and taking velocity moments of the Boltzmann equation. This yields conservation equations for the mass, momentum, and energy of each species. The collisional terms are typically modeled by assuming a Maxwellian velocity distribution function. Viscosity plays a negligible role, and its effect is usually not included in the momentum equations. Maxwell's equations are solved to determine the electric and magnetic fields generated by the charged particles and their motion. In the absence of an externally imposed magnetic field, magnetic effects are generally quite small, and the plasma is usually treated as electrostatic, where the electric field is the gradient of a potential, $E = -\partial\Phi/\partial x$.

In this report, three species are considered: the background gas (He), the ions (He^+), and the electrons. The background gas is assumed to be stagnant and at constant temperature (300 K) and pressure (250 mTorr). Since the ion mass is very nearly the same as the mass of the background gas, the ions are assumed to be in thermal equilibrium with the background, and no energy equation is solved for the ions. Due to their lower mass, the electrons exchange kinetic energy very poorly with the other particles, and their temperature can be significantly higher than the other species. Thus, it is important to solve for the electron energy. A commonly used simplification to the electron momentum equation is the "drift–diffusion approximation." The electron inertial terms, *i.e.*, those in the material derivative, are neglected. This results in a balance between the Lorentz force, the pressure gradient, and the drag from collisions with the background gas, which yields an algebraic expression for the electron flux.

2.1.1 Governing equations

The above assumptions provide the following fluid equations (Nitschke & Graves 1994). The variables n_e and n_i denote the electron and ion number densities, respectively, and v_i and $\frac{3}{2}n_e k_B T_e$ represent the ion velocity and the electron thermal energy density. The electron number density and thermal fluxes are represented by j_e and q_e. The density of the neutrals is denoted by N, and Φ and E denote the electric potential and electric field, respectively. Note that the ion momentum equation (1d) should, strictly speaking, have the term $-Nn_e k_{i0} e^{-E_a/k_B T_e}\, v_i/n_i$ on the right-hand side; however, the magnitude of this term is small, and it is often neglected.

$$\frac{\partial n_e}{\partial t} + \frac{\partial j_e}{\partial x} = N n_e k_{i0} e^{-E_a/k_B T_e} \tag{1a}$$

$$j_e = -\frac{1}{k_{mt} N m_e}\left(e n_e E + \frac{\partial (n_e k_B T_e)}{\partial x}\right) \tag{1b}$$

$$\frac{\partial n_i}{\partial t} + \frac{\partial (n_i v_i)}{\partial x} = N n_e k_{i0} e^{-E_a/k_B T_e} \tag{1c}$$

$$\frac{\partial v_i}{\partial t} + v_i \frac{\partial v_i}{\partial x} = \frac{eE}{m_i} - \frac{\pi}{2} N \sigma_{cx} |v_i|\, v_i \tag{1d}$$

$$\frac{\partial(\frac{3}{2}n_e k_B T_e)}{\partial t} + \frac{\partial q_e}{\partial x} = -ej_e E - h_{iz} N n_e k_{i0} e^{-E_a/k_B T_e} - 3\frac{m_e}{m_{neut}} N k_{mt} n_e k_B (T_e - T_{neut}) \quad (1e)$$

$$q_e = \frac{5}{2} j_e k_B T_e - \frac{5 n_e k_B T_e}{2 m_e k_{mt} N} \frac{\partial(k_B T_e)}{\partial x} \quad (1f)$$

$$\frac{\partial^2 \Phi}{\partial x^2} = -\frac{e}{\epsilon_0}(n_i - n_e) \quad (1g)$$

Equations (1a)-(1g) are non-dimensionalized prior to solution. The plasma bulk is used to define reference values for the charged particle densities (n_0) and the electron temperature (T_0). For the simulations discussed in this report, these values are 1.0×10^{15} m^{-3} and $45,000K$, respectively. The Debye length ($\lambda_e = \sqrt{\epsilon_0 k_B T_0 / e^2 n_0}$) and plasma frequency ($\omega_p = \sqrt{e^2 n_0 / \epsilon_0 m_e}$) are used as reference length and time scales, respectively. The non-dimensional form of the equations, using the same notation as for the dimensional equations, is shown below with the non-dimensionalizing parameters.

$$\frac{\partial n_e}{\partial t} + \frac{\partial j_e}{\partial x} = p_1 n_e \, e^{-p_2/T_e} \quad (2a)$$

$$j_e = -p_7 \left(n_e E + \frac{\partial(n_e T_e)}{\partial x} \right) \quad (2b)$$

$$\frac{\partial n_i}{\partial t} + \frac{\partial(n_i v_i)}{\partial x} = p_1 n_e \, e^{-p_2/T_e} \quad (2c)$$

$$\frac{\partial v_i}{\partial t} + v_i \frac{\partial v_i}{\partial x} = p_3 E - p_4 |v_i| \, v_i \quad (2d)$$

$$\frac{\partial(\frac{3}{2}n_e T_e)}{\partial t} + \frac{\partial q_e}{\partial x} = -j_e E - p_5 n_e e^{-p_2/T_e} - p_6 n_e (T_e - T_{neut}) \quad (2e)$$

$$q_e = \frac{5}{2} j_e T_e - p_8 n_e T_e \frac{\partial T_e}{\partial x} \quad (2f)$$

$$\frac{\partial^2 \Phi}{\partial x^2} = -(n_i - n_e) \quad (2g)$$

The variables p_1 through p_8 are defined as follows:

$$p_1 = N k_{i0} 2\pi/\omega_p \qquad p_2 = E_a/k_B T_0$$
$$p_3 = e^2 n_0 4\pi^2 / m_i \epsilon_0 \omega_p^2 \qquad p_4 = N \sigma_{cx} \lambda_e \pi / 2$$
$$p_5 = h_{iz} N k_{i0} 2\pi / k_B T_0 \omega_p \qquad p_6 = 3 m_e N k_{mt} 2\pi / m_{neut} \omega_p$$
$$p_7 = 2\pi e^2 n_0 / \omega_p k_{mt} N m_e \epsilon_0 \qquad p_8 = 5 p_7 / 2$$

2.1.2 Boundary conditions

Characteristic analysis of the governing equations was performed to determine the number of boundary conditions required. For the electron equations, the analysis

showed that boundary conditions should be specified on both sides of the computational domain. The boundary conditions used in this report are the same as those used by Nitschke & Graves (1994); they are applied on both sides of the domain:

$$j_e = \mp \frac{n_e}{4}\sqrt{\frac{8k_BT_e}{\pi m_e}}(1-\Theta) \tag{2h}$$

$$q_e = \frac{5}{2} j_e k_B T_e \tag{2i}$$

The boundary fluxes for the electron continuity equation (2a) are assumed to correspond to the one-way flux for particles with a Maxwellian velocity distribution. Reflection is accounted for with Θ; a value of 0.25 (Nitschke & Graves 1994) was used. The thermal flux at the boundaries is equated to the enthalpy flux (2i). A boundary condition for the energy equation (2e) that is more consistent with the boundary condition for the continuity equation is to equate q_e to the one-way flux of kinetic energy for a Maxwellian distribution, $\frac{4}{3} \times \frac{3}{2} k_B T \times j_e$, or $q_e = 2 j_e k_B T_e$. Our simulations showed little difference between the two; however, for consistency with Nitschke & Graves (1994), the enthalpy flux boundary condition (2i) is used in this report.

Characteristic analysis of the ion equations indicated that no boundary conditions should be specified. The characteristics point in the direction of v_i, and, since E is always directed out of the plasma close to the walls, the ions always flow out of the computational domain. Thus, no boundary conditions are given for the ion equations. Nitschke & Graves (1994) applied $\partial n_i/\partial x = 0$ on both boundaries and set $\partial v_i/\partial x = 0$ on one boundary. When these boundary conditions were used, small oscillations in the ion number density were observed at both boundaries. When the boundary conditions were removed, so were the oscillations. Results demonstrating this will be shown in section 2.3.5.

The boundary conditions for the Poisson equation (2g) are a sinusoidal radio-frequency voltage on the left side of the domain and ground on the right side. The amplitude of the voltage is 500 V, and the frequency is 12 MHz. The spacing between the electrodes is 4 cm. These conditions were chosen to correspond with the calculations of Nitschke & Graves (1994).

2.2 Numerical method

The dependent variables are discretized on a non-uniform, staggered grid. A staggered grid was chosen because of the conservative properties it provides for the non-linear fluid equations (Harlow & Welch 1965). Figure 2 illustrates the staggered positioning of variables. The equations governing n_e and n_eT_e are quite stiff, and an implicit time advancement scheme is therefore necessary. The ion equations do not exhibit such stiffness, and an explicit time advancement scheme is adequate. The spatial and temporal discretization are described below.

2.2.1 Spatial discretization

The following discrete equations were used to advance the dependent variables in the interior of the domain. Note that a skew-symmetric form of the convection term is used in the ion momentum equations.

FIGURE 2. Storage locations of variables on the non-uniform, staggered grid.

Ion continuity:

$$\frac{d\,n_{i,k}}{dt} = -\left(\frac{2}{\Delta x_{k-1}+\Delta x_k}\right)\left[\left(\frac{n_{i,k}+n_{i,k+1}}{2}\right)v_{i,k+1/2} - \left(\frac{n_{i,k-1}+n_{i,k}}{2}\right)v_{i,k-1/2}\right] + p_1 n_{e,k}\, e^{-p_2/T_{e,k}} \tag{3}$$

Ion momentum:

$$\frac{d\,v_{i,k+1/2}}{dt} = -\frac{1}{2}\left[v_{i,k+1/2}\left(\frac{\tilde{v}_{i,k+1}-\tilde{v}_{i,k}}{\Delta x_k}\right) + \frac{1}{2}\frac{\tilde{v}_{i,k+1}^2-\tilde{v}_{i,k}^2}{\Delta x_k}\right] + p_3 E_{k+1/2} - p_4|v_{i,k+1/2}|\,v_{i,k+1/2} \tag{4}$$

$$\tilde{v}_{i,k} = \frac{\Delta x_k\, v_{i,k-1/2} + \Delta x_{k-1}\, v_{i,k+1/2}}{\Delta x_{k-1}+\Delta x_k}$$

Electron continuity:

$$\frac{d\,n_{e,k}}{dt} = -\left(\frac{2}{\Delta x_{k-1}+\Delta x_k}\right)(j_{e,k+1/2}-j_{e,k-1/2}) + p_1 n_{e,k}\, e^{-p_2/T_{e,k}} \tag{5}$$

The discretization of j_e significantly impacts the robustness of the solution, and is discussed in detail in section 2.3.

Electron energy:

$$\begin{aligned}\frac{3}{2}\frac{d\,n_e T_{e,k}}{dt} =& -\left(\frac{2}{\Delta x_{k-1}+\Delta x_k}\right)(q_{e,k+1/2}-q_{e,k-1/2}) \\ & -\frac{1}{2}\left(j_{e,k-1/2}E_{k-1/2} + j_{e,k+1/2}E_{k+1/2}\right) \\ & - p_5 n_{e,k}\, e^{-p_2/T_{e,k}} - p_6 n_{e,k}(T_{e,k}-T_{neut}) \\ q_{e,k+1/2} =& \frac{5}{2} j_{e,k+1/2} T_{e,k+1/2} \\ & - p_8\left(\frac{n_e T_{e,k+1}+n_e T_{e,k}}{2}\right)\left(\frac{T_{e,k+1}-T_{e,k}}{\Delta x_k}\right)\end{aligned} \tag{6}$$

FIGURE 3. Schematic of the full Jacobian for the discretized electron equations; the large X's indicate numbers with magnitudes much larger than those shown by small x's. The structure of the Jacobian indicates that the functional dependence of the electron variables at the k^{th} location on the electron variables outside the $k-1$ to $k+1$ range is weak.

2.2.2 Temporal discretization

A 4^{th} order Runge-Kutta method is used to advance the ion equations; implicit time advancement is used for the electrons. Both fully nonlinear and linearized time advancement methods for the electron equations (5 and 6) were considered. Of the fully implicit methods, the implicit Euler and trapezoidal methods were evaluated. The implicit Euler method was found to perform better; oscillatory solutions were obtained with the trapezoidal method unless very small time steps were used. A Newton-Raphson iterative technique was used to solve the equations resulting from the fully nonlinear formulation. Strictly speaking, the Jacobian for this system is a nearly full matrix since both the continuity and energy equations involve the electric field, which is an elliptic function involving the net charge density. Thus, the equations for $n_{e,k}^{n+1}$ and $n_e T_{e,k}^{n+1}$ are functions of $n_{e,1}^{n+1}, n_{e,2}^{n+1}, \ldots, n_{e,N-1}^{n+1}, n_{e,N}^{n+1}$.

However, close examination of the Jacobian matrix reveals that the sub-matrices which are more than one block off the main diagonal have terms that are much smaller in magnitude than the sub-matrices on the main diagonal and those immediately adjacent to it (see Fig. 3). Since the Jacobian is used in the iterative solution of the system of equations, this indicates that blocks not adjacent to the main diagonal have little impact on the solution at sub-iterations. Thus, the full

Jacobian can be approximated by a block, tri-diagonal Jacobian. The results obtained with the reduced Jacobian are virtually the same as the results with the full Jacobian, and the time savings is significant ($O(N)$ operations versus $O(N^2)$ with an iterative solver).

The electrons can also be advanced in time with a linearized implicit algorithm. Such algorithms for the implicit Euler, trapezoidal, and implicit Runge-Kutta methods (Zhong 1996) were considered. As before, the Euler method is more stable than the linearized trapezoidal method. The second order linearized implicit Runge-Kutta scheme seems to offer the same stability as the linearized Euler, but with higher order accuracy. While cheaper per time-step than the fully nonlinear formulation, the linearized algorithms require a smaller time step for both stability and accuracy. A detailed comparison between the time advancement methods is shown in section 2.3.4.

2.3 Simulation results

The stiff nature of the electron equations makes even one-dimensional simulations challenging. The non-dimensional n_e and n_eT_e vary widely over the course of a radio-frequency period, from a minimum of $\mathrm{O}(10^{-55})$ to a maximum of O(1). The ion variables are much better behaved, with n_i between O(0.1) and O(1) and $|v_i|$ no greater than O(1). Roughly 500 radio-frequency periods are needed to reach a harmonic quasi-steady-state. The discretization of j_e has a significant impact on the stability and accuracy of the solution. Sections 2.3.1 and 2.3.2 discuss some commonly used approaches. A non-dissipative discretization based upon rearranging the expression for j_e is derived in section 2.3.3 and shown to possess a good combination of robustness and accuracy. Time-advancement of the electron equations is discussed in section 2.3.4. Finally, section 2.3.5 shows how imposing boundary conditions on the ions can cause point-to-point oscillations.

2.3.1 Symmetric interpolation

This is the most straightforward discretization of j_e, which is computed as follows:

$$j_{e,k+1/2} = -p_7 \left[\left(\frac{n_{e,k} + n_{e,k+1}}{2} \right) E_{k+1/2} + \frac{n_e T_{e,k+1} - n_e T_{e,k}}{\Delta x_k} \right] \tag{7}$$

While this is a natural approach, it turns out that it requires very fine grids to capture the wide spatial variations in n_e and n_eT_e. Even with a stretched grid, at least about 400 grid points are required. At this resolution, the minimum grid spacing is about 3% of a Debye length, and the maximum (in the plasma bulk) is nearly half a Debye length. Using fewer grid points results in unphysical negative values for n_e or n_eT_e in the sheath regions (where these two variables become extremely small), making the computation unstable. The fine grid required by the electron equations causes the calculation to take a prohibitively long time — nearly 2 hours on an SGI Iris Indigo 2 (500 steps per period for 500 periods) — which makes solving this type of problem in three dimensions impractical. Assuming that roughly 100 grid points would be needed for the other two dimensions means that a three dimensional calculation would take 10,000 times longer, or about two and a quarter

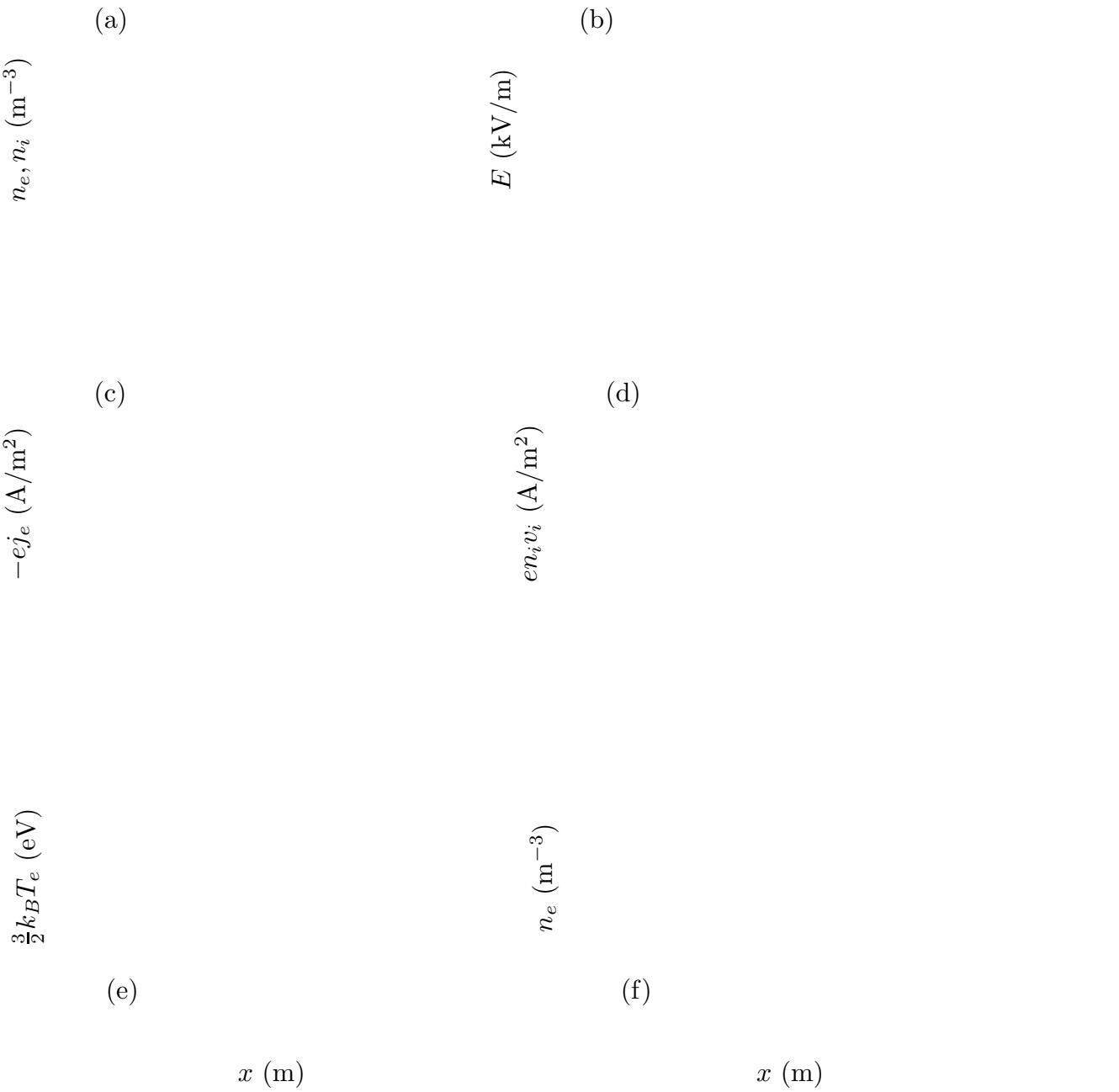

FIGURE 4. The plasma variables at several times during the radio-frequency period (T): 0.5T (——), 0.675T (- - - -), 0.75T (—·—), and 0.875T (·····). The variables plotted are: (a) electron number density along with the ion number density (•), which essentially does not change throughout the period; (b) the electric field; (c) the electron current; (d) the ion current; and (e) the electron thermal energy, $\frac{3}{2}k_BT_e$. To demonstrate the drastic rarefaction in the electron number density, the spatial variation at 0.75T is plotted on a logarithmic scale in (f). The electron energy density has a similar variation.

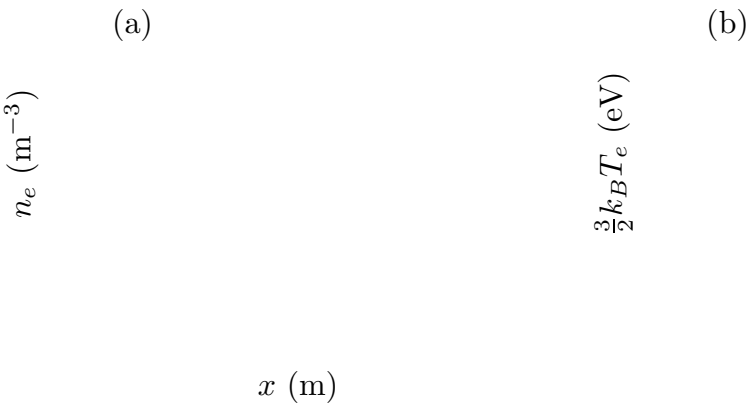

FIGURE 5. Upwinded calculations as a function of grid resolution: 200 points (·····), 400 points (—·—), and 800 points (– – – –). For comparison, the "exact" calculation with 400 points (———) is also shown. All of these computations were performed with the same size time step (500 steps per radio frequency period) for the same duration (500 periods) while starting from the same initial condition.

years, on the same computer, assuming (optimistically) that the computation time would still depend linearly on the number of grid points.

Simulation results, using 1,000 steps per period and the fully implicit Euler method for the electron advancement, are shown in Fig. 4. Grid independence of the plotted solutions was established; these results will be referred to as the "exact" results. The results are virtually identical to those of Nitschke and Graves (1994) for the same conditions (background gas at 250 mTorr, applied radio-frequency voltage of 500 V at 12 MHz with a gap of 4 cm). These solutions were used as a benchmark to evaluate alternative discretizations which are discussed below.

2.3.2 Upwinded interpolation

One approach to increase the stability of the discretized equations and reduce the number grid points is to use upwinding. This can drastically reduce the minimum number of grid points needed for a computation, and the calculation time can be dropped to a few minutes. For example, with 20 grid points and 100 time steps per period, a solution is obtained in about 3 minutes. This brings a three-dimensional calculation within reach. Not surprisingly, upwinding is used quite extensively in processing plasma simulations (Sommerer & Kushner 1992; Gogolides *et al.* 1992, and Kushner *et al.* 1996).

We evaluate an upwinded approach similar to that used in Barnes, *et al.* 1987. The sign of the electric field at $x_{k+1/2}$ determines the discretization of the drift component of the electron flux. All the other variables are calculated in the same fashion as before.

$$j_{e,k+1/2} = \begin{cases} -p_7 \left[n_{e,k} E_{k+1/2} + \frac{n_e T_{e,k+1} - n_e T_{e,k}}{\Delta x_k} \right], & \text{if } E_{k+1/2} < 0 \\ -p_7 \left[n_{e,k+1} E_{k+1/2} + \frac{n_e T_{e,k+1} - n_e T_{e,k}}{\Delta x_k} \right], & \text{if } E_{k+1/2} > 0 \end{cases} \tag{8}$$

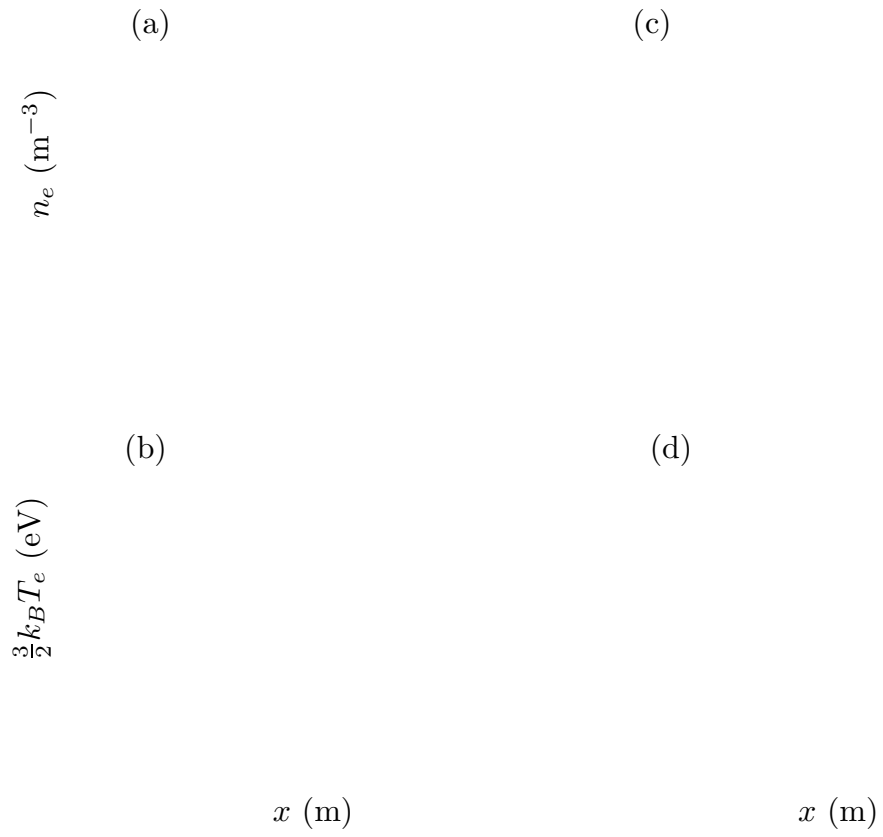

FIGURE 6. Comparison between the upwinded method and the electron velocity method. The upwinded calculations are plotted in (a) and (b); the electron velocity method calculations are plotted in (c) and (d). The grids used in these plots have: 400 points, the "exact" solution (———); 40 points (– – – –); and 20 points (—·—). All the simulations were performed with the same size time step (1,000 steps per radio frequency period) for the same duration (500 periods) while starting from the same initial condition. The same grid spacing was used for both the upwinded simulation and the electron velocity based solution on the 20 and 40 point grids.

Although more robust, this approach is not as accurate as the symmetric/central-difference technique discussed previously. For the same grid as the "exact" calculation, the upwinded calculation still shows grid dependence (see Fig. 5). Also, considerable error is observed with coarse grids (Fig. 6).

2.3.3 A non-dissipative flux discretization

An alternative approach that is non-dissipative yet robust is derived below. The drift-diffusion approximation is rearranged and then integrated to determine the mean electron velocity. Since the electron flux, j_e, equals $n_e v_e$, where v_e is the electron velocity, the drift-diffusion equation (2b) can be divided by n_e and rearranged

x (m)

FIGURE 7. Influence of spatial discretization on accuracy. The results shown are from the "exact" solution (———), the electron velocity method with 20 points (– – – –), and the upwinded method with 20 points (—·—).

via the chain and product rules to yield:

$$v_e = -p_7 \left(E + T_e \frac{\partial \ln n_e}{\partial x} + \frac{\partial T_e}{\partial x} \right) \tag{9}$$

With the electric field expressed as the gradient of the potential, Eq. (9) can be integrated from x_k to x_{k+1}. Using the midpoint rule for the $T_e \partial \ln n_e / \partial x$ term yields the following expression for the mean electron velocity:

$$\bar{v}_{e,k+1/2} = -p_7 \left[-\frac{\Phi_{k+1} - \Phi_k}{\Delta x_k} + \frac{T_{e,k+1/2}}{\Delta x_k} \ln \frac{n_{e,k+1}}{n_{e,k}} + \frac{T_{e,k+1} - T_{e,k}}{\Delta x_k} \right] \tag{10}$$

The temperature gradient is commonly neglected in the drift-diffusion representation of j_e. However, this is inappropriate. The first term and the second term in Eq. (10), though much larger in magnitude than the third term, cancel with each other to a large extent, particularly in the sheath region. Their sum is comparable in magnitude to the temperature gradient term.

The electron flux at the midpoint is now simply the product of the average velocity and the average number density.

$$j_{e,k+1/2} = \bar{v}_{e,k+1/2} \left(\frac{n_{e,k} + n_{e,k+1}}{2} \right) \tag{11}$$

The results from two upwinded calculations and two calculations with the new method (henceforth referred to as the electron velocity method) are shown in Fig. 6. The electron velocity technique, which is non-dissipative, closes in very quickly on the "exact answer," while the upwinded method is quite far from grid convergence. In the sheath region there is a slight discrepancy in T_e between the electron velocity method and the "exact" solution. However, recall that the variables actually being

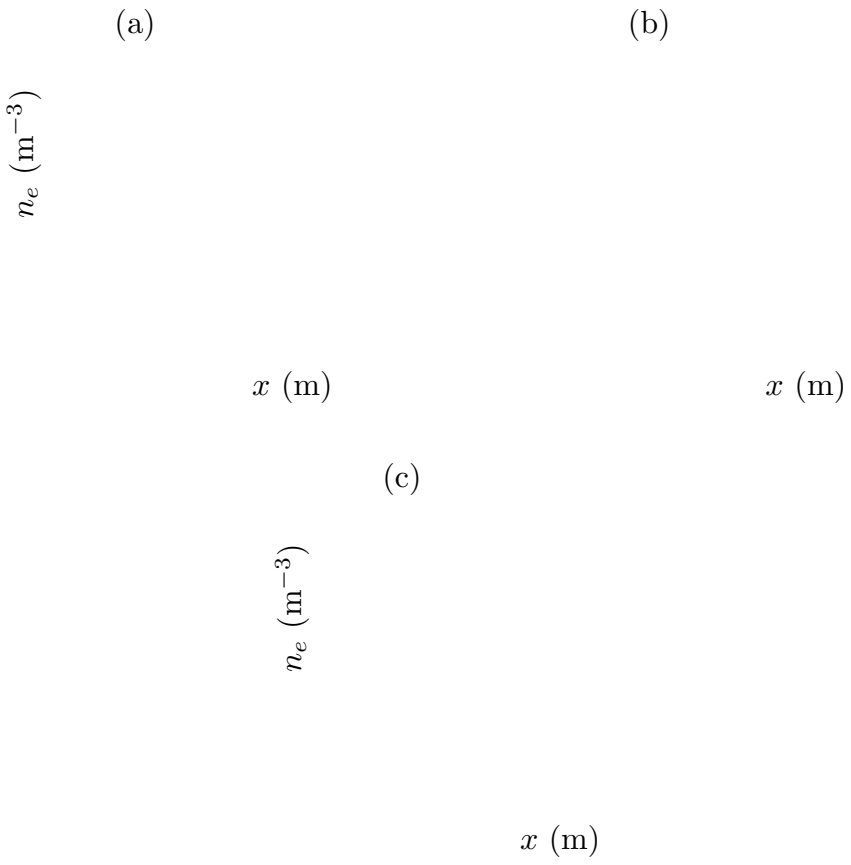

FIGURE 8. Comparison between the time advancement methods. The fully implicit Euler results are plotted in (a), the linearized implicit Euler results in (b), and the linearized implicit second order Runge-Kutta in (c). Three different time steps were used for each method: 4,000 steps per period (———), 2,000 (- - - -), and 1,000 (—·—). The same grid and initial conditions were used for all the runs. All plots show the electron number density profile after 500 periods.

solved for are n_e and n_eT_e, both of which are very nearly zero in the sheath; the electron energy is found from the ratio of the two. Figure 7 shows the large error with the upwinded calculation in the sheath regions.

This revised discretization for the electron flux makes a three-dimensional calculation practical. The 20 point calculation shown in Fig. 6 had a run time of slightly less than 10 minutes on an SGI Iris Indigo 2 (the same computer and same optimization level as that used for the 400 point symmetric interpolation calculation).

2.3.4 Alternative time advancement

Two alternatives to the fully implicit Euler algorithm for the electron time advancement were evaluated: linearized implicit Euler and linearized implicit Runge-Kutta (second order). Figure 8 illustrates the sensitivity of these approaches to the time-step size. In general, the linearized approaches take less time per timestep

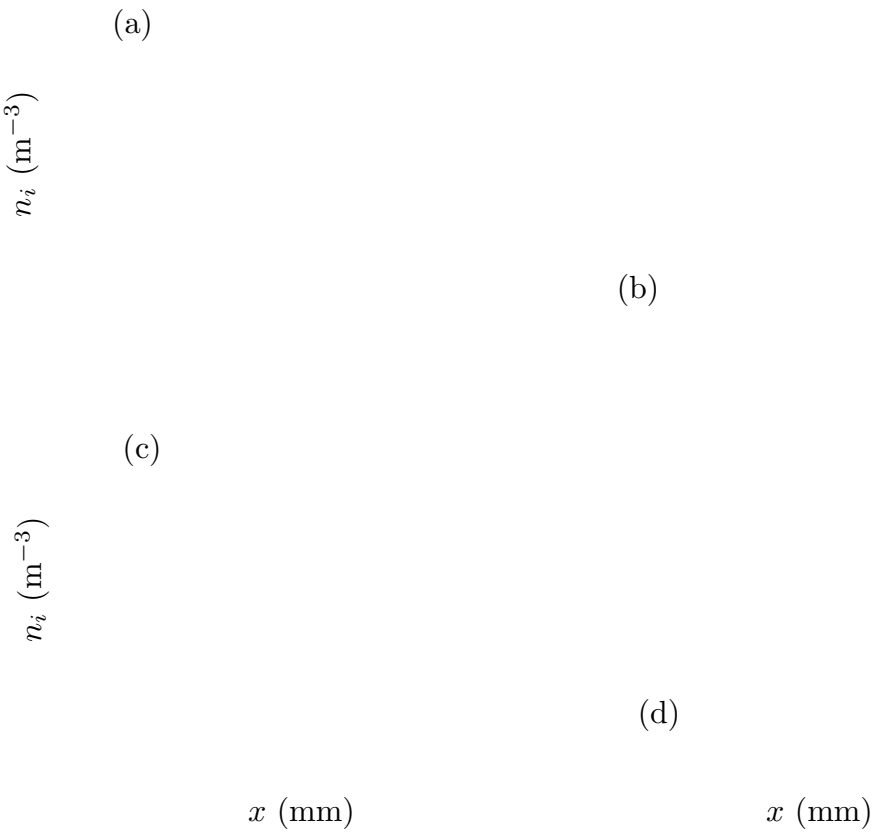

FIGURE 9. An illustration of the impact of boundary conditions on n_i. Calculations were performed on a uniform grid with 100 points in (a) and (b), and with 200 points in (c) and (d). Shown are the left and and right edges of the domain in each case without (———) and with (- - - -) boundary conditions.

when compared to the fully nonlinear formulation. However, the error associated with linearization requires that the timestep be smaller to achieve the same accuracy as the nonlinear formulation. The net result is that the linearized implicit Euler method requires more CPU time to achieve the same level of accuracy, while the second order linearized implicit Runge-Kutta requires about the same CPU time as the fully implicit formulation. The run times for the various methods and step sizes are shown in Table 1.

2.3.5 Impact of ion boundary conditions

A characteristic analysis of the ion equations was performed to determine the validity of the boundary conditions used by Nitschke and Graves. The analysis indicated that no boundary conditions should be enforced. The effect of imposing boundary conditions is shown in Fig. 9. The $\partial n_i/\partial x = 0$ boundary condition used by Nitschke and Graves is enforced by setting $n_{i,1} = n_{i,2}$ and $n_{i,N} = n_{i,N-1}$. The $\partial v_i/\partial x = 0$ boundary condition on the left side is enforced by setting $v_{i,1} = v_{i,3/2}$. With the boundary conditions imposed, oscillations in n_i are observed close

Time advancement	*Time steps per period*	*Approximate run time (minutes)*
Fully implicit	4,000	25
Euler	2,000	14
	1,000	9.5
Linearized implicit	4,000	9
Euler	2,000	4.5
	1,000	2
Linearized implicit	4,000	13
Runge-Kutta	2,000	6.5
	1,000	3.5

TABLE 1. Run times for various electron time advancement methods. All computations were performed on the same grid (20 points) for the same duration (500 periods) with the same initial condition.

to the boundaries. Simulations were performed on uniform grids of 100 and 200 points, and, despite the increase in resolution, the point-to-point oscillations are still evident. When the boundary conditions are removed, so are the oscillations.

3. Future plans

A three-dimensional solver using the algorithm derived in this report is being developed. The solver will be capable of simulating both inductively coupled, as well as capacitively coupled plasmas. Non-Maxwellian effects in the electrons, simple chemistry, and effects due to dust particles will be included. When completed, the solver will be used to explore the impact of dust contaminants on the plasma.

Acknowledgments

The authors gratefully acknowledge many helpful discussions with Prof. M. A. Cappelli.

REFERENCES

BARNES, M. S., COLTER, T. J., & ELTA, M. E. 1987 Large-signal time-domain modeling of low-pressure rf glow discharges. *J. Appl. Phys.* **61,** 81-89.

GOGOLIDES, E., SAWIN, H. H., & BROWN, R. A. 1992 Direct calculation of time-periodic states of continuum models of radio-frequency plasmas. *J. Chem. Engng. Sci.* **47,** 3839-3855.

GRILL, A. 1994 *Cold Plasma in Materials Fabrication.* IEEE Press.

HARLOW, F. H. & WELCH, J. E. 1965 Numerical calculation of time-dependent viscous incompressible flow of fluid with free surface. *Phys. Fluids.* **8,** 2182-2189.

HERSHKOWITZ, N. 1998 Role of Plasma-aided manufacturing in semiconductor fabrication. *IEEE Trans. Plasma Sci.* **26,** 1610-1620.

Kushner, M. J. 1996 Advances in plasma equipment modeling. *Solid State Techn.* **39,** No. 6**,** 135-144.

Kushner, M. J., Collison, W. Z., Grapperhaus, M. J., Holland, J. P., & Barnes, M. S. 1996 A three-dimensional model for inductively coupled plasma etching reactors: Azimuthal symmetry, coil properties, and comparison to experiments. *J. Appl. Phys.* **80,** 1337-1344.

Lieberman, M. A. & Lichtenberg, A. J. 1994 *Principles of plasma discharges and materials processing.* John Wiley & Sons, Inc.

Nitschke, T. E. & Graves, D. B. 1994 A comparison of particle in cell and fluid model simulations of low-pressure radio frequency discharges. *J. Appl. Phys.* **76,** 5646-5660.

Sommerer, T. J. & Kushner, M. J. 1992 Numerical investigation of the kinetics and chemistry of rf glow discharge plasmas sustained in He, N_2, O_2, $He/N_2/O_2$, $He/CF_4/O_2$, and SiH_4/NH_3 using a Monte Carlo-fluid hybrid model. *J. Appl. Phys.* **71,** 1654-1673.

Zhong, X. 1996 Additive Semi-Implicit Runge-Kutta methods for computing high-speed nonequilibrium reactive flows. *J. Comput. Phys.* **128,** 19-31.